

DNA Tension Probes Show that Cardiomyocyte Maturation Is Sensitive to the Piconewton Traction Forces Transmitted by Integrins

Sk Aysha Rashid, Aaron T. Blanchard, J. Dale Combs, Natasha Fernandez, Yixiao Dong, Hee Cheol Cho, and Khalid Salaita*



Cite This: <https://doi.org/10.1021/acsnano.1c04303>



Read Online

ACCESS |



Metrics & More



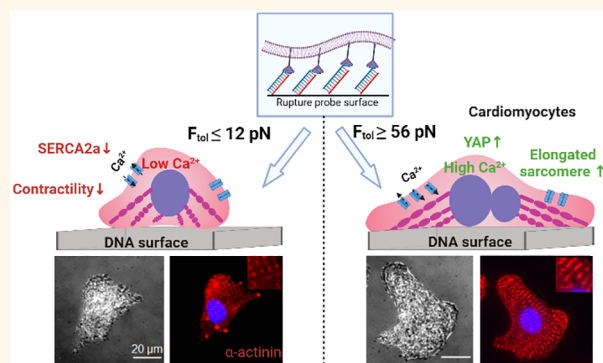
Article Recommendations



Supporting Information

ABSTRACT: Cardiac muscle cells (CMCs) are the unit cells that comprise the heart. CMCs go through different stages of differentiation and maturation pathways to fully mature into beating cells. These cells can sense and respond to mechanical cues through receptors such as integrins which influence maturation pathways. For example, cell traction forces are important for the differentiation and development of functional CMCs, as CMCs cultured on varying substrate stiffness function differently. Most work in this area has focused on understanding the role of bulk extracellular matrix stiffness in mediating the functional fate of CMCs. Given that stiffness sensing mechanisms are mediated by individual integrin receptors, an important question in this area pertains to the specific magnitude of integrin piconewton (pN) forces that can trigger CMC functional maturation. To address this knowledge gap, we used DNA adhesion tethers that rupture at specific thresholds of force (~ 12 , ~ 56 , and ~ 160 pN) to test whether capping peak integrin tension to specific magnitudes affects CMC function. We show that adhesion tethers with greater force tolerance lead to functionally mature CMCs as determined by morphology, twitching frequency, transient calcium flux measurements, and protein expression (F-actin, vinculin, α -actinin, YAP, and SERCA2a). Additionally, sarcomeric actinin alignment and multinucleation were significantly enhanced as the mechanical tolerance of integrin tethers was increased. Taken together, the results show that CMCs harness defined pN integrin forces to influence early stage development. This study represents an important step toward biophysical characterization of the contribution of pN forces in early stage cardiac differentiation.

KEYWORDS: DNA sensors, rupture probes, integrin forces, cardiomyocyte's maturation, substrate stiffness, pN forces, integrin mechanotransduction



The development of the heart is a complex and dynamic process that can be categorized into two main phases. The first is differentiation of neonatal stem cells into various cardiac cell lineages such as cardiac progenitor cells and cardiac crescent cells.^{1–3} The second is subsequent maturation of these lineages into functional cells such as fibroblasts, as well as different types of mature cardiac muscle cells (CMCs) which achieve rhythmic beating.⁴ Maturation is the final phase of this dynamic process where the CMCs undergo extensive structural, functional, and metabolic changes as the heart develops from the fetal to adult stage.^{5–7} Developing a fundamental understanding of CMC maturation is important

as it impacts many areas including the development of therapies to treat heart disease. For example, during a major cardiac insult, the heart can lose an enormous number of cardiomyocytes.⁸ As a treatment, current therapeutic strategies are heavily focused on repairing the damaged tissue using

Received: May 20, 2021

Accepted: February 11, 2022

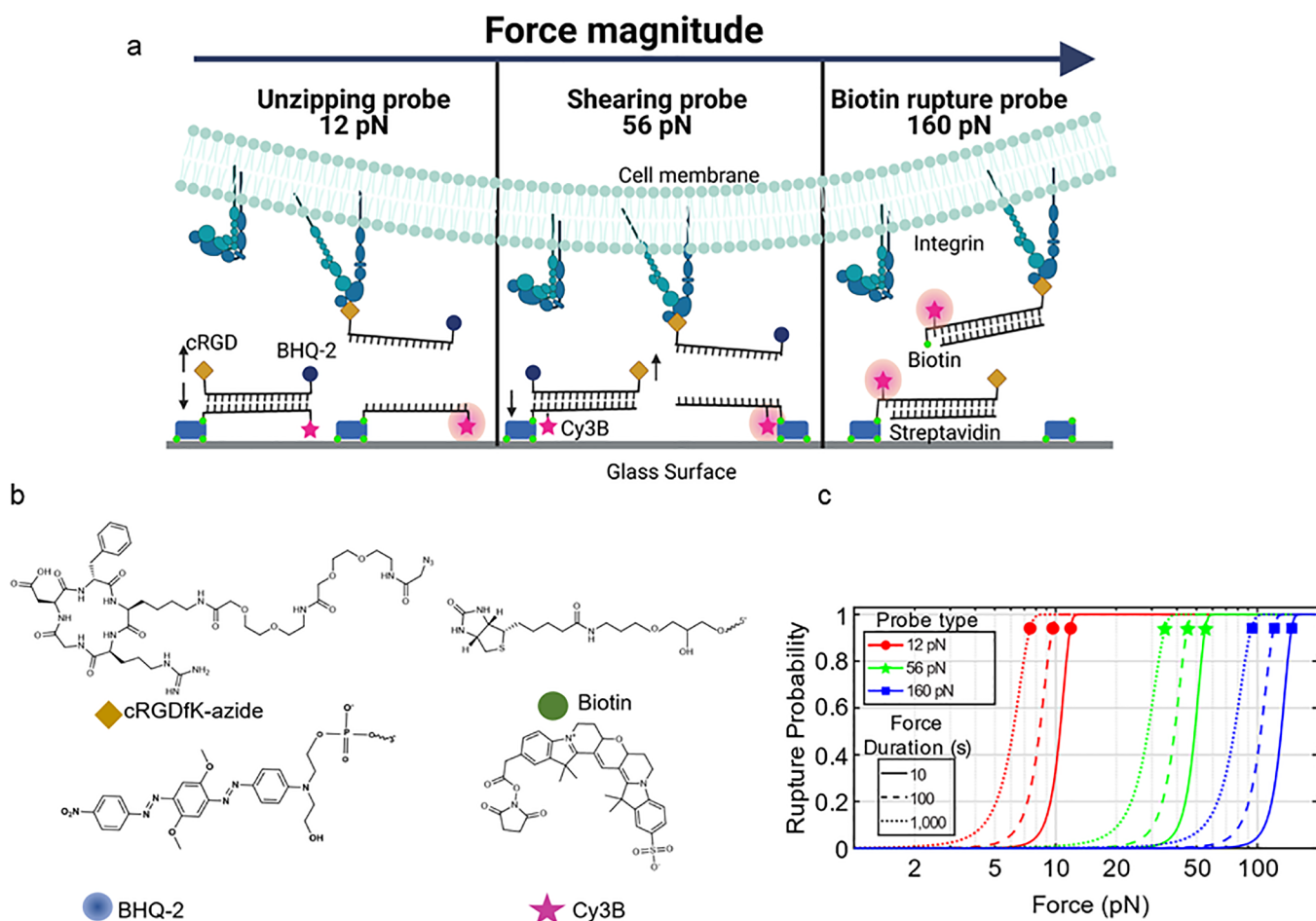


Figure 1. DNA probes to control CMC integrin tension. (a) Schematic representation of cardiac muscle cells (CMCs) pulling on the varied threshold of rupture probe surfaces 12, 56, and 160 pN. The scheme shows the oligonucleotides used in the work where 12 and 56 pN probes have the same chemical composition but different orientations of the biotin group anchoring the probe to the surface. For 160 pN probes, the same strand presents the biotin and RGD groups. (b) Chemical structures of modification to oligonucleotides used to construct rupture probes and (c) rupture probability of probes under different loading times.

cardiac lineage stem cells.^{9–11} However, this approach tends to exhibit limited efficacy as only a small fraction (~3%) of the therapeutic stem cells mature appropriately.^{12,13} The mechanisms of CMC maturation remain unclear, and hence, a major motivation for studying this process is to improve CMC potency as a therapeutic for myocardial regeneration.^{14–17}

A key area of particular interest is understanding how physical and biochemical cues can alter and influence CMC developmental fate.^{18–20} While there is a significant body of literature investigating how different chemical cues can modulate CMC fate, there is relatively less known about the role of mechanical cues in controlling maturation despite evidence that it influences development and function of heart tissue.^{4,11,21} Irregularities in mechanotransduction can result in stiffening of the cardiac tissue, a precursor to multiple cardiac diseases, such as cardiac fibrosis, congenital heart defects, and arrhythmia.^{14,22} Therefore, developing tools to better understand how mechanical cues modulate CMC function is critical to improving the efficacy of stem-cell based therapeutics.

Prior studies of neonatal rat ventricular myocytes (NRVM), a subtype of CMC, have reported that CMCs display greater yields of functional maturation showing higher peak calcium, aligned sarcomeres, and higher expression of the associated proteins on surfaces with the appropriate Young's mod-

ulus.^{19,23–29} One of the most studied markers of maturation is the sarcomere, the fundamental unit of mechanical contractility in CMCs. Each mature sarcomere consists of actin filaments and sarcomeric α -actinin proteins, with elongated and aligned z-lines.^{19,23,32} Another marker of CMC maturation is the SERCA2a calcium pump which tunes the rate of calcium transport and hence the amplitude and frequency of calcium transients. These reports show a link between substrate stiffness and CMC function, indicating the importance of adhesion receptor mechanotransduction in CMC maturation.^{32,33}

To study how mechanical cues influence CMC maturation, the field has generally measured CMC maturation for cells grown on hydrogels of differing stiffness.^{19,23,24} Past work showed a “goldilocks”-like relation between substrate stiffness and CMC maturation, where intermediate levels of substrate stiffness enhanced functional maturation of CMCs.^{18,19,24} For example, NRVM cells cultured on PDMS gels matured optimally when the substrate stiffness was 10–20 kPa as quantified using different markers such as CMC morphology, SERCA2a, YES associated protein (YAP), and myosin heavy chain (MHC) expression as well as sarcomeric organization and Ca^{2+} signaling.^{19,24,25,43,44} This demonstrates how tuning bulk mechanical properties, like stiffness, controls cardiomyo-

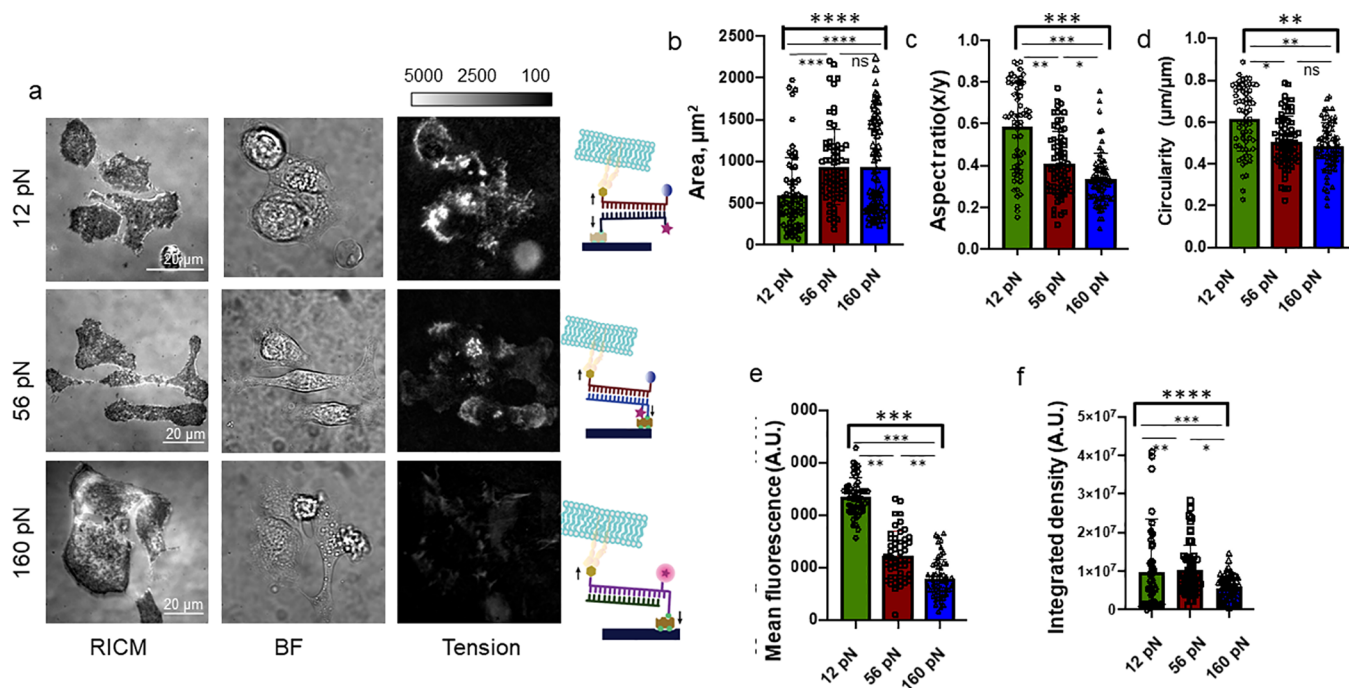


Figure 2. Cardiomyocytes display elongated morphology with integrin–ligand tension > 12 pN. (a) Representative images of CMCs (live) on 12, 56, and 160 pN rupture probe surfaces; the leftmost panel (RICM) channel shows the outline of the attached cells, and the middle panel (bright field), TRITC channel, shows the signal increase of Cy3B fluorescence due to probe rupture for 12 and 56 pN probes and the inverted fluorescence loss for 160 pN probes ($t = 6–8$ h). (b–f) Bar graphs showing the spread area, aspect ratio (x/y), circularity, and mean fluorescence under the cells and integrated fluorescent density obtained from CMCs that were cultured on 12, 56, and 160 pN probes. Each data point represents a single cell while the bar shows the average. ****, ***, **, *, and ns indicate $p < 0.0001$, $p < 0.001$, $p < 0.01$, $p < 0.05$, and not significant, respectively, as determined from one-way ANOVA. Error bars show standard deviation for $n > 3$, where each experiment was averaged from three or more different cell isolations with three different sets of surface preparations. Scale bar = $20 \mu\text{m}$.

cyte maturation through a mechanosensing response. However, all past work in this area has focused on tuning the bulk mechanical properties of the substrate, and it remains unknown how the force magnitude transmitted through individual adhesion receptors contributes to the events of CMC maturation.^{19,23,32,33} Therefore, a remaining challenge in this area is to manipulate the traction forces applied by CMCs with molecular resolution (piconewton, pN) and to study how these individual molecular forces modulate maturation.

Here, we address this challenge by using cell adhesion ligands that can rupture mechanically at different thresholds. We use variants of the tension gauge tether (TGT) and the biotin–streptavidin rupture tether to control the maximum threshold of integrin tension and to study how these thresholds control CMC maturation.^{30,31,34,35} We find that CMC integrins show sensitivity to pN forces ranging from ~ 12 pN–160 pN, thereby modulating their maturation fate. The findings suggest that CMCs can sense pN forces through their adhesion receptors, and threshold forces that exceed 12 pN lead to functional maturation, elongated morphology, synchronized twitching, and more coordinated Ca^{2+} peaks. Integrin threshold forces greater than 12 pN also lead to increased expression of proteins associated with contractility such as SERCA2a and YAP. This report represents a step toward studying the relationship of pN integrin forces and functional maturation of cardiomyocytes.

RESULTS AND DISCUSSION

DNA Probes to Control CMC Integrin Tension. The rupture probes we used here are comprised of a DNA duplex

anchored to a surface using a “bottom” oligonucleotide that is complementary to a “top” strand presenting an integrin ligand. In this work, we used the cyclic arginine-glycine-aspartic acid-D-phenylalanine-lysine (cRGDfK) ligand (Figure 1b) which mimics fibronectin and primarily binds to the $\alpha_5\beta_1$ and $\alpha_v\beta_3$ integrin receptors.³⁶ These integrin receptors are highly expressed by neonatal cardiac cells and shown to be important for development and growth.^{37–43} Additionally, neonatal cardiomyocytes display the greatest adhesion to fibronectin compared to that of collagen and laminin.⁴⁴ Therefore, the cRGDfK peptide (referred to as the RGD-ligand) was ideally suited for our current investigation of neonatal cardiomyocytes. When the rupture probes experience mechanical forces that exceed their tension tolerance (T_{tol}), the DNA duplex will rupture, thus terminating the mechanotransduction between the integrin and ligand. In this way, the rupture probes cap the maximum tension experienced by the integrin receptor. Importantly, the magnitude of the T_{tol} is time-dependent and can be tuned from ~ 12 pN up to ~ 56 pN (for a 2 s force duration) by changing the location of the anchoring group on the bottom strand relative to the ligand position on the top strand (Figure 1).³⁰ For example, TGT probes with the ligand and the anchoring groups on the same terminus of the duplex have a $T_{\text{tol}} = 12$ pN, while shearing probes that present the ligand and anchoring groups on opposite ends of the duplex display a $T_{\text{tol}} = 56$ pN (Figure 1a). To record probe rupture events, we conjugated the anchor strand with a fluorophore (Cy3B), while the ligand strand was conjugated with a quencher (BHQ2) (Figures S1 and S2, Supporting Information Tables 1 and 2). With this fluorophore–quencher pair, mechanical melting of the duplex results in a turn-on signal

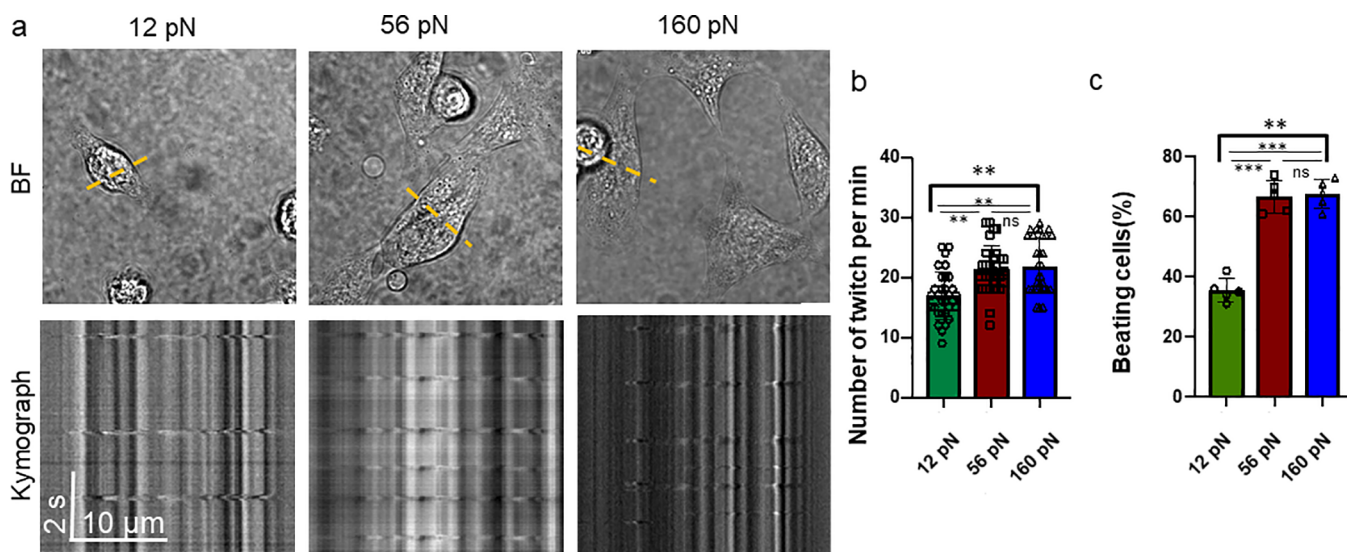


Figure 3. Cardiomyocytes displayed a contractile profile consistent with greater maturation on surfaces with $T_{\text{tol}} = 56$ and 160 pN. (a) Brightfield images from time-lapse of cardiomyocytes twitching on different probes ($t = 8\text{--}10$ h); the dashed yellow line shows the major axis of the kymograph. (b) Kymographs of representative cells along the yellow dashed line. The y -axis of the graphs is elapsed time (t), and x shows the displacement, $t = 2$ s, $x = 10$ μm . (c) Bar graphs showing the average number of twitches per cell for each replicate. Ten 1 min long videos were analyzed in BF; the error bar shows the standard deviation for $n = 3$. The error bar shows the standard deviation for $n = 3$. ****, ***, **, *, and ns indicate $p < 0.0001$, $p < 0.001$, $p < 0.01$, $p < 0.05$, and not significant, respectively, as determined from one-way ANOVA. (d) Bar graph showing the percentage of attached cells measured from 11 videos per replicate, calculated by the percentage of cells that had contractility; the error bar shows the standard error of the mean for $n = 5$. Scale bar = 10 μm .

with a 10-fold enhancement in fluorescence intensity (Figure S3).³¹

This fluorescence intensity reports on the accumulation of mechanical events with $F > T_{\text{tol}}$. To extend the T_{tol} to greater values, we designed another type of duplex where the RGD–ligand strand is directly anchored to the surface. Because the probe is anchored using biotin–streptavidin, we estimate an effective T_{tol} (2 s) of ~ 160 pN (Figure 1c).⁴⁵ All three types of DNA probe surfaces were prepared from streptavidin-modified glass slides and yielded nearly identical probe densities of ~ 1400 molecules/ μm^2 (Figure S4). Most prior studies using TGTs use T_{tol} values estimated using a 2 s duration, but in our case, given that CMC maturation occurs over longer durations (\sim hours), we plotted the expected T_{tol} for longer time durations in Figure 1c (SI Method 1). Assuming that the applied force magnitude is steady, the 2 s T_{tol} values of 12, 56, and 160 pN reported previously are shifted to 6, 28, and 80 pN, respectively, for the 1000 s time duration. We still refer to the 2 s T_{tol} values in the text for clarity but with the understanding that the actual applied forces may vary drastically based on the mechanical history of the bond given that cell forces are highly dynamic.

Cardiomyocytes Display Elongated Morphology with Integrin–Ligand Tension > 12 pN. In our work, we used neonatal rat CMCs as a model for CMC maturation. This is a well-studied and established model of CMC maturation.^{4,19,23,24} We first used CMC morphology as an indicator of maturation. This is because the CMC spreading area and cell shape are correlated with maturation. CMCs grow by elongating,^{19,21,23} which facilitates the arrangement of contractile proteins in CMCs and results in enhanced contraction capabilities.^{4,11} Moreover, the morphology of CMCs is easily measured and strongly correlated to their maturation and fate.

Initially, we screened the seeding density of these cells to identify an optimal density of 38 000–45 000 cells/ cm^2 .

Images were taken at 2 h intervals to measure spreading and the initiation of beating/twitching. To investigate the influence of morphology on cell function we waited for the cardiac cells to start beating and imaged cells to measure the spread area, aspect ratio, and circularity (Figure 2a–d). We observed that CMCs display twitching $\sim 6\text{--}8$ h after seeding on these rupture probe surfaces regardless of T_{tol} and used this time point to measure cell morphology. We found that cells adhered poorly on the 12 pN T_{tol} surface compared to the 56 and 160 pN probe surfaces, and we generally found fewer attached cells on the 12 pN surfaces (Figure 2a). Moreover, cells were more elongated on 56 and 160 pN surfaces and had an average spreading area of ~ 900 μm^2 , significantly greater (ANOVA, $P < 0.001$) than cells on 12 pN substrates (Figure 2b). Aspect ratio and circularity measurements confirmed that CMCs were more elongated on the 56 and 160 pN surfaces compared to the 12 pN surface (Figure 2c,d).

We also measured the fluorescence intensity under each cell as a quantitative readout of the accumulated mechanical events where $F > T_{\text{tol}}$ under the cell (Figure S5). Note that this signal is a lower bound estimate of the tension signal as there is DNA loss due to the activity of nucleases and proteases and due to the inherent k_{off} rate of biotin–streptavidin⁴⁵ (Figure S6). Representative fluorescence images show that the weaker 12 pN rupture probe displayed greater fluorescence and more dissociation (2.5-fold difference) compared to the 56 pN rupture probes (Figure 2e). For the 160 pN probes, we fluorescently tagged the biotinylated strand and hence the readout is a loss of signal due to disassociation of the biotin–streptavidin bond (Figure 2e,f).⁴⁵ We observed that CMCs generate a tension signal prior to initiating twitching/beating (Figure S7). This tension signal did not abruptly increase due to twitching, thus indicating that the forces generated by twitching fail to significantly drive probe rupture (12, 56, and 160 pN probes). This suggests that CMC twitching generates

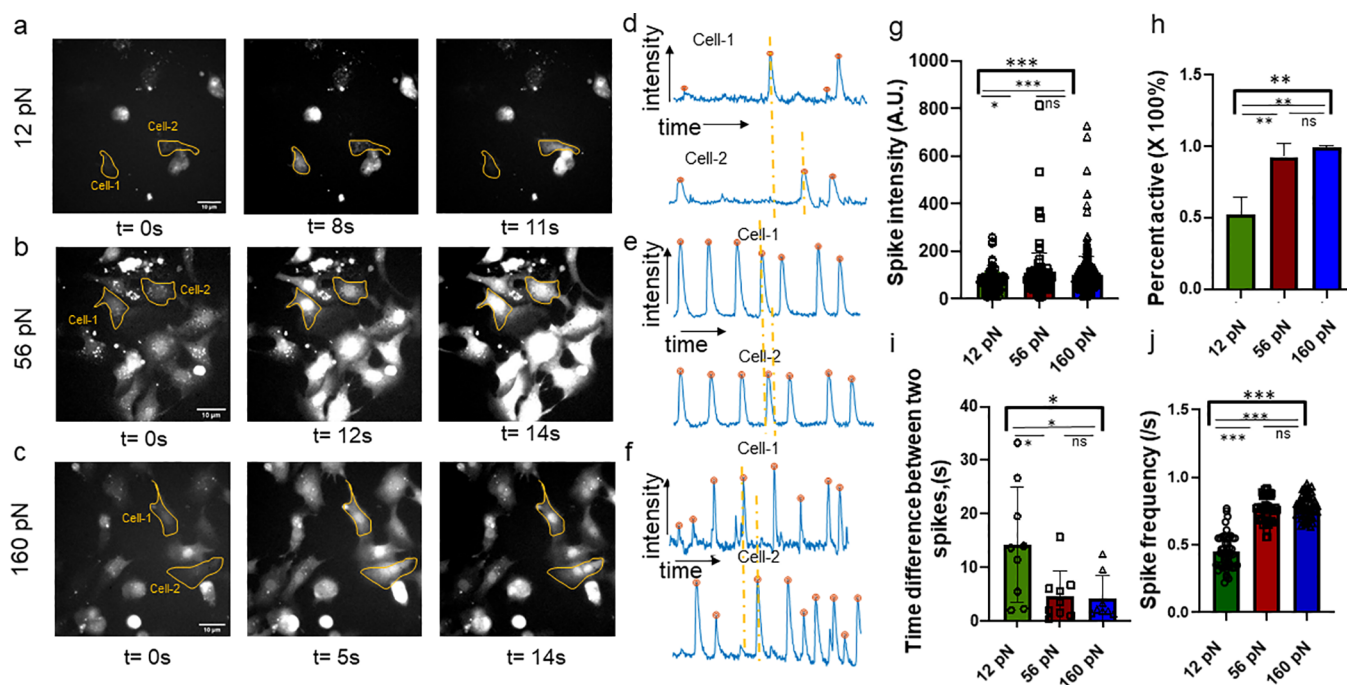


Figure 4. Cardiomyocytes displayed a calcium profile consistent with greater maturation on surfaces with $T_{\text{tot}} = 56$ and 160 pN. (a–c) FITC images of CMCs on 12, 56, and 160 pN rupture probes stained with Fluo-4. Images were taken from the time-lapse to measure the transient Ca^{2+} sparks ($t = 12$ –14 h). (d–f) Transient Ca^{2+} flux profile of the outlined CMCs on 12, 56, and 160 pN probes. The dotted yellow line shows if the Ca^{2+} sparks have the same τ for the outlined cells. (g–j) Bar graph showing spike intensity, percent active, the time difference between two spikes (each data point represents a video where $n > 10$ cells were analyzed for each data point), and spike frequency obtained from Fluo-4-stained CMCs on 12, 56, and 160 pN probes. ****, ***, **, *, and ns indicate $p < 0.0001$, $p < 0.001$, $p < 0.01$, $p < 0.05$, and not significant, respectively, as determined from one-way ANOVA. Scale bar = 10 μm .

weaker tension than that of cell adhesion. In general, we found that the spatial distribution of integrin tension for the 56 pN rupture probes was localized at the center of the cells in fluorescent tension puncta (Figure 2a) with nuclear staining, showing the location to be around the nucleus (Figure S8). The tension signal seems inconsistent with the cytoskeleton and adhesion structures because DNA probe rupture is irreversible; hence, the tension signal represents a history of past mechanical events (Figure S9). In order to confirm the change in morphology and tension is due to integrin mechanotransduction, we treated the cells with eptifibatid, RGD binding integrin inhibitor,⁴⁶ for 30 min before seeding. The cells had no difference in morphology, and their tension was significantly reduced (70–75%) (Figure S10), suggesting the phenomenon observed here is directly connected with integrin mechanotransduction. To evaluate the role of the ROCK and myosin II pathways, we treated the cells with y-27632 (Rho kinase inhibitor) and blebbistatin (myosin II inhibitor). Drug-treated CMCs had similar morphology and cell spread area regardless of the probe T_{tot} (Figures S11 and S12). When we compared the control (untreated) CMCs to those of the drug-treated CMCs, we found that the cell on the 12 pN probes showed a 2-fold greater spread area and significantly lowered tension signal as a result of myosin II inhibition. This has been noted in previous studies and is likely the result of loss of rigidity sensing mechanisms.^{23,27} We also investigated the effect of ligand density in force sensing of CMC by controlling the ligand density (Figure S13). This experiment confirmed the ligand loss or differential ligand densities among 12, 56, and 160 pN surfaces is not the major reason for poor attachment or differences in functional maturation of CMCs on 12 pN surfaces.

Cardiomyocytes Display Contractile Behavior and Calcium Profiles Consistent with Greater Maturation on Surfaces with $T_{\text{tot}} = 56$ and 160 pN.

Compared to other muscle cells, cardiac muscle cells are distinctive in their ability to generate synchronized beating and spontaneous twitching. As CMCs mature, the magnitude and frequency of CMCs is often used as another parameter to quantify maturation.^{24,25} To characterize the twitching rate in our experiments, neonatal rat cardiomyocytes were plated on rupture surfaces with different T_{tot} values. Cells displayed spontaneous twitching on all rupture probe surfaces tested at 8 h after seeding. However, we did note that spontaneous twitching could be observed at shorter time points (4–6 h) for $T_{\text{tot}} = 56$ and 160 pN. Twitch frequencies for individual cells were measured using kymographs obtained from time-lapse videos of CMCs (Figure 3a,b). The axis of twitching was assigned based on the direction of the twitch, which was typically the long axis of the cells, and then the twitch frequency was calculated by measuring the time interval of contraction and dividing it by the time frame (Figure S14). We found that CMCs have higher twitching frequencies on 56 and 160 pN surfaces (Figure 3c). Moreover, a significantly (ANOVA, $P < 0.005$) greater population of CMCs were twitching and exhibited spontaneous beating (synchronized twitching within neighboring cells) on the 56 pN and 160 pN rupture probe compared to 12 pN substrates (Figure 3d and SI Videos 1–3).

Calcium (Ca^{2+}) is a critical intrinsic modulator of functional cardiomyocytes and plays a role in connecting the electrical signals which illicit muscle contraction and rhythmic beating of the heart, gene transcription, and various other functions. Previous studies showed that CMCs had higher transient Ca^{2+}

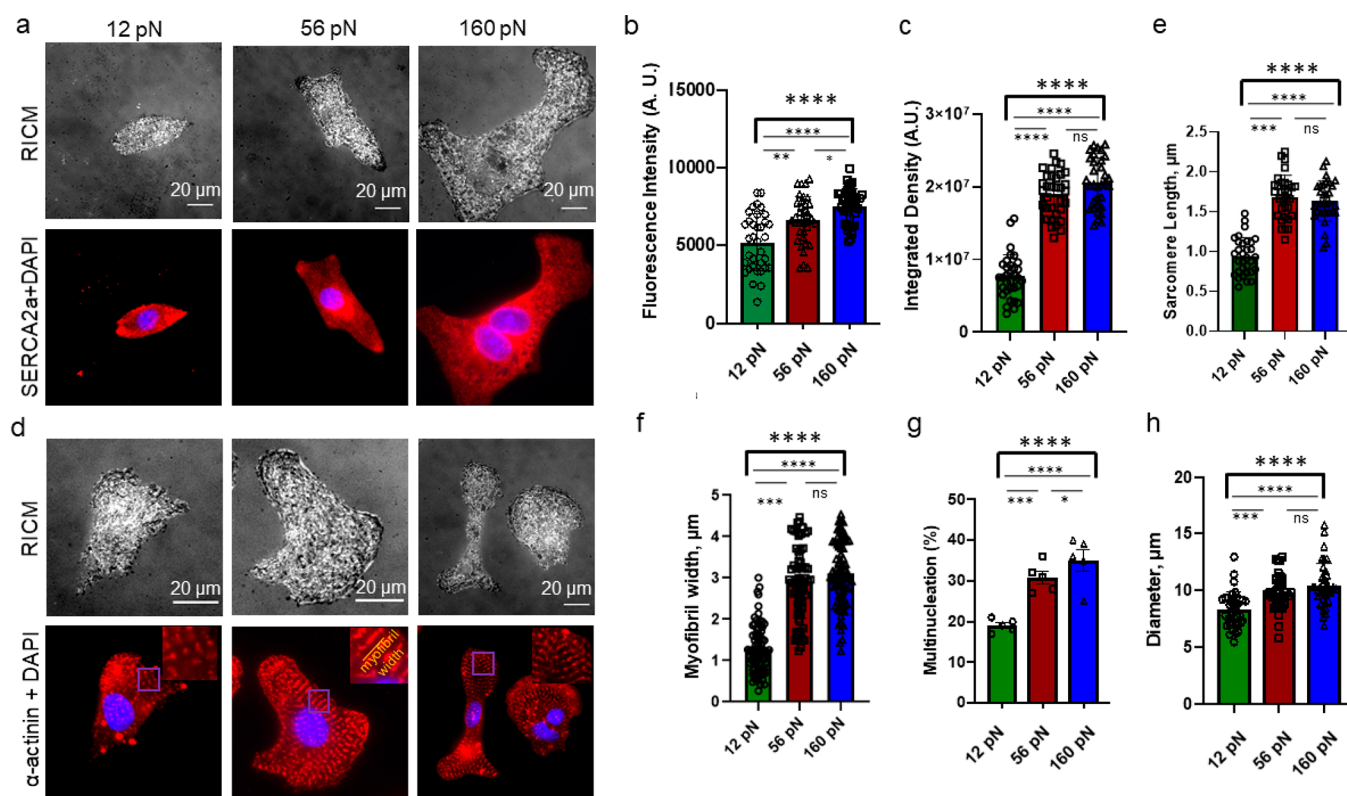


Figure 5. Cardiomyocytes having aligned sarcomeres at higher integrin force. (a) RICM of representative cells on the 12, 56, and 160 pN surfaces along with overlay immunostaining images showing SERCA2a (red) and DAPI (blue) staining ($t = 10\text{--}12$ h). Plots showing (b) the average SERCA2a expression and (c) total SERCA2a expression, as measured from immunostaining images. (d) RICM and sarcomeric α -actinin immunostaining of representative cells on the 12, 56, and 160 pN surfaces. The inset highlights the myofibril widths (z-band), and the yellow dashed line shows the length of individual z bands. Plots of (e) sarcomere length and (f) myofibril width for CMCs cultured on 12, 56, and 160 pN probes. For (a) through (f), each data point represents one cell, and data was obtained from three biological replicates where each replicate included analysis of $n > 15$ cells. (g) and (h) show plots of percentage of cells containing multiple nuclei and average nuclear diameter, respectively. $n = 5$ independent replicates. ****, ***, **, *, and ns indicate $p < 0.0001$, $p < 0.001$, $p < 0.01$, $p < 0.05$, and not significant, respectively, as determined from one-way ANOVA. Error bars show the standard deviation, where each independent experiment used cells obtained from cells pooled from >20 animals with three different sets of surface preparations. Scale bar = $20\ \mu\text{m}$.

flux and more regular spikes on 10 kPa PDMS substrates compared to 5 and 50 kPa.^{23,24} To evaluate the Ca^{2+} response as a function of the T_{tot} , cells were grown on the substrates for ~ 8 h and then were stained with the Fluo-4 Ca^{2+} indicator for 2 h. After dye incubation, transient Ca^{2+} spikes which coincided with twitching were measured by time-lapse videos in the Fluo-4 channel (Figure 4a–c and SI Videos 4–6). The spike intensities were significantly higher in 56 and 160 pN substrates compared to that of 12 pN (Figure 4d–f,g). CMCs also had more synchronized Ca^{2+} spikes on 56 and 160 pN substrates with more cells exhibiting spontaneous beating (Figure 4h–j). This shows that integrin traction forces greater than 12 pN contribute to more contractile and matured Ca^{2+} profiles in CMCs.

Cardiomyocytes Have Aligned Sarcomeres at a Higher Integrin Force. A CMC's functional maturation is closely related to the spatial organization of the sarcoplasmic reticulum (SR), which harbors key elements for calcium cycling, such as RyR channels that release Ca^{2+} and SERCA2a pumps for Ca^{2+} uptake.^{47,48} Specifically, elongation and alignment of the SR indicates CMC maturation.^{24,32,49} Moreover, recent studies have shown that SERCA2a organization is substrate dependent, and the expression levels is upregulated in functional CMCs.^{24,32,49,50}

To understand how molecular cell traction forces influence the SERCA2a expression, we plated the CMCs on different rupture probe surfaces with varied T_{tot} . As described above, cells were incubated on the 12, 56, and 160 pN DNA rupture surfaces for 6–8 h. The cells were then fixed and stained with a SERCA2a antibody. It was observed that SERCA2a was clustered around the nucleus on the 56 and 160 pN surfaces in contrast to the 12 pN surfaces which were more diffuse (Figure 5a). Quantification of the total SERCA2a from fluorescence microscopy images showed that the total and average SERCA2a expression was significantly higher (2–3-fold greater) on the 56 pN and 160 pN substrates compared to the 12 pN substrates (Figure 5b,c). It was also observed that SERCA2a organization was different in CMCs seeded on the 12 pN surface compared to 56 and 160 pN surfaces (Figure S15). This data is aligned with the previous work that shows SERCA2a enhancement on CMCs plated on a gel of optimal substrate stiffness (~ 10 kPa).²³

To measure the SR morphology, CMCs were seeded on rupture probes and stained for sarcomeric α -actinin. Fluorescence microscopy showed CMCs with organized and aligned SR on 56 pN and 160 pN surfaces, which contrasts with the 12 pN surfaces that displayed disorganized and punctate sarcomeric α -actinin (Figure 5e). The total expressions of α -actinin were not found to be different

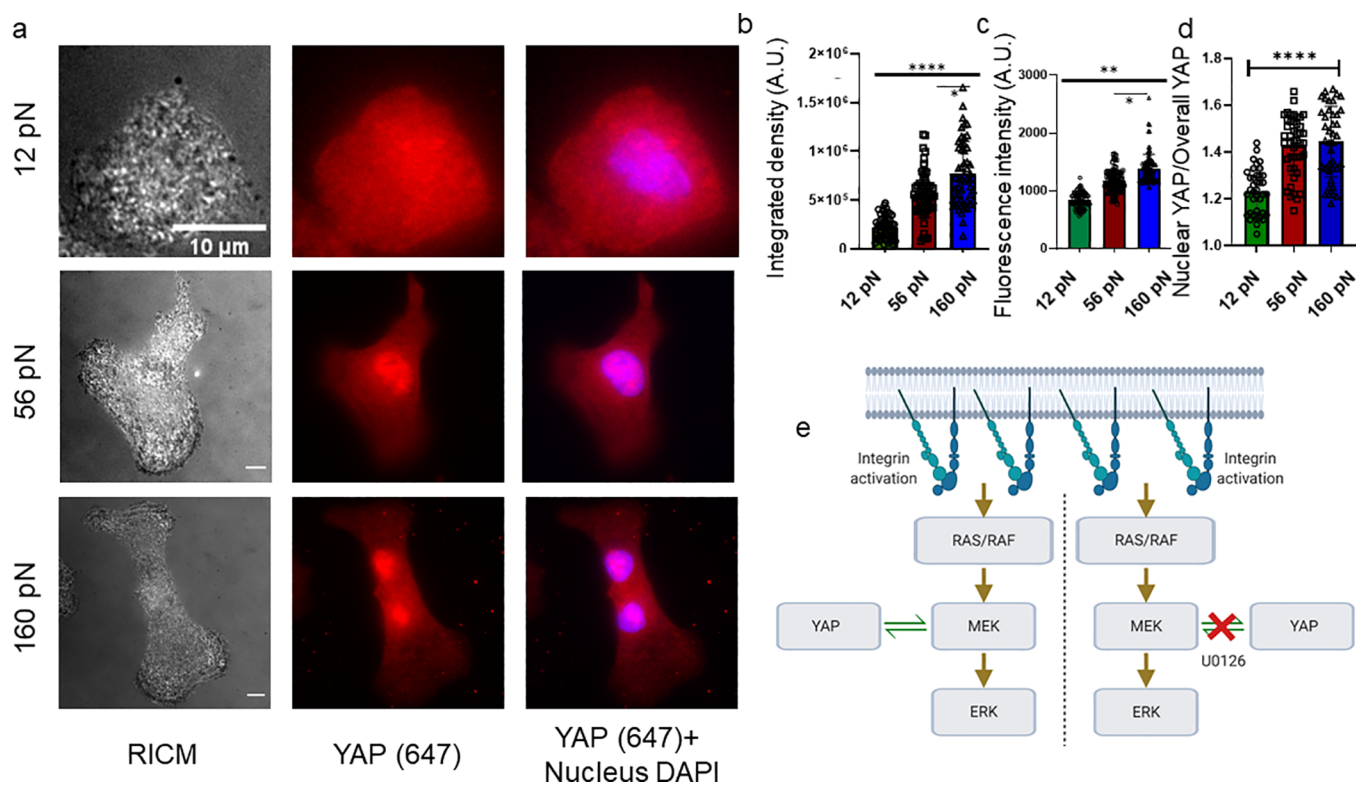


Figure 6. YES, associated protein (YAP), is upregulated when integrin $F > 12$ pN. (a) RICM, YAP, and DAPI immunostaining of representative cells on the 12, 56, and 160 pN surfaces ($t = 12$ –14 h). (b) Total expression of YAP measured by immunostaining ($t = 8$ –10 h). (c) Average YAP expression ($t = 8$ –10 h). (d) Fraction of nuclear YAP expression over total cellular YAP expression ($t \geq 12$ –14 h); each data point represents a single cell while the bar shows the average. ****, ***, **, *, and ns indicate $p < 0.0001$, $p < 0.001$, $p < 0.01$, $p < 0.05$, and not significant, respectively, as determined from one-way ANOVA. Error bars show standard deviation for $n > 3$, where each experiment was averaged from three or more different cell isolations with three different sets of surface preparations. Scale bar = 10 μm . (e) Proposed mechanism of YAP upregulation due to integrin activation.

among the different thresholds of rupture (Figure S16), which is consistent with previous studies growing CMCs on gels of differing Young's moduli. Upon measuring the length of the z-band known as myofibril width and sarcomere length, the stained CMCs showed almost 2-fold longer myofibril width and SR length on 56 and 160 pN surfaces compared to 12 pN surfaces (Figure 5d–f). The total number of α -actinin bands measured by particle tracking showed lower numbers for CMCs plated on the 12 pN surface compared to the 56 and 160 pN surfaces (Figure S16). These data show nearly identical cell responses on the 56 and 160 pN probe surfaces in contrast to the 12 pN surface and thus suggest that integrin forces > 12 pN result in more mature SR organization in CMCs, which is essential for CMC function.

Even though adult CMCs are mostly mononucleated, they have been shown to have multinucleation in postnatal development stage.^{51,52} Multinucleation and polyploidy have been reported as essential for the CMC cell cycle and early development.^{53–55} We observed CMCs have increased amounts of multinucleation when the receptor and ligand attachment is more stable. CMCs showed an increased nuclear diameter, eccentricity, area, and multinucleation on 56 and 160 pN surfaces compared to the 12 pN surfaces (Figure 5g,h and Figure S17). We hypothesize this to arise from the greater T_{tol} of the receptor bond on 56 and 160 pN TGTs facilitating better attachment of multinucleated CMCs.

YAP Is Upregulated When Integrin $F > 12$ pN. YAP is a well-known transcription co-activator that is mechanosensitive

and regulated by integrin mechanotransduction.^{56–58} Past reports showed upregulated nuclear YAP translocation with increasing ECM rigidity in various cell lines.⁵⁹ YAP plays an important role in the HIPPO pathway, which controls the proliferation of CMCs and is important in controlling organ development during mammalian gestation. Increased YAP expression is essential in early CMC differentiation, which presents an increasing need to understand the role of YAP in CMC maturation.^{50,60,61} A recent study using human induced pluripotent stem cell derived cardiomyocytes (hiPSC-CMs) observed higher nuclear YAP levels for cells cultured on stiffer substrates compared to softer substrates for CMCs.⁵⁰

We examined YAP upregulation and nuclear translocation using immunofluorescence and found upregulated YAP expression on 56 and 160 pN compared to the 12 pN rupture probes (Figure 6a,b and Figure S18). However, no difference in YAP nuclear/cytosolic ratio was observed across all the surfaces tested after 8–10 h of attachment (Figure S18). These results were surprising, as previous studies observed YAP nuclear translocation in nonmyocytes as well as in stem cell derived CMCs.⁵⁰ To validate our conclusion, we incubated CMCs on the rupture probe surfaces for additional time (10–12 h, 12–14 h, and 14–16 h). We observed CMCs to have higher nuclear YAP on 56 and 160 pN surfaces compared to the 12 pN probe when incubated on the surface for a prolonged period (12–14 h) (Figure 6d).

This suggests YAP translocation is highly dynamic and requires a longer incubation time. Additionally, we measured

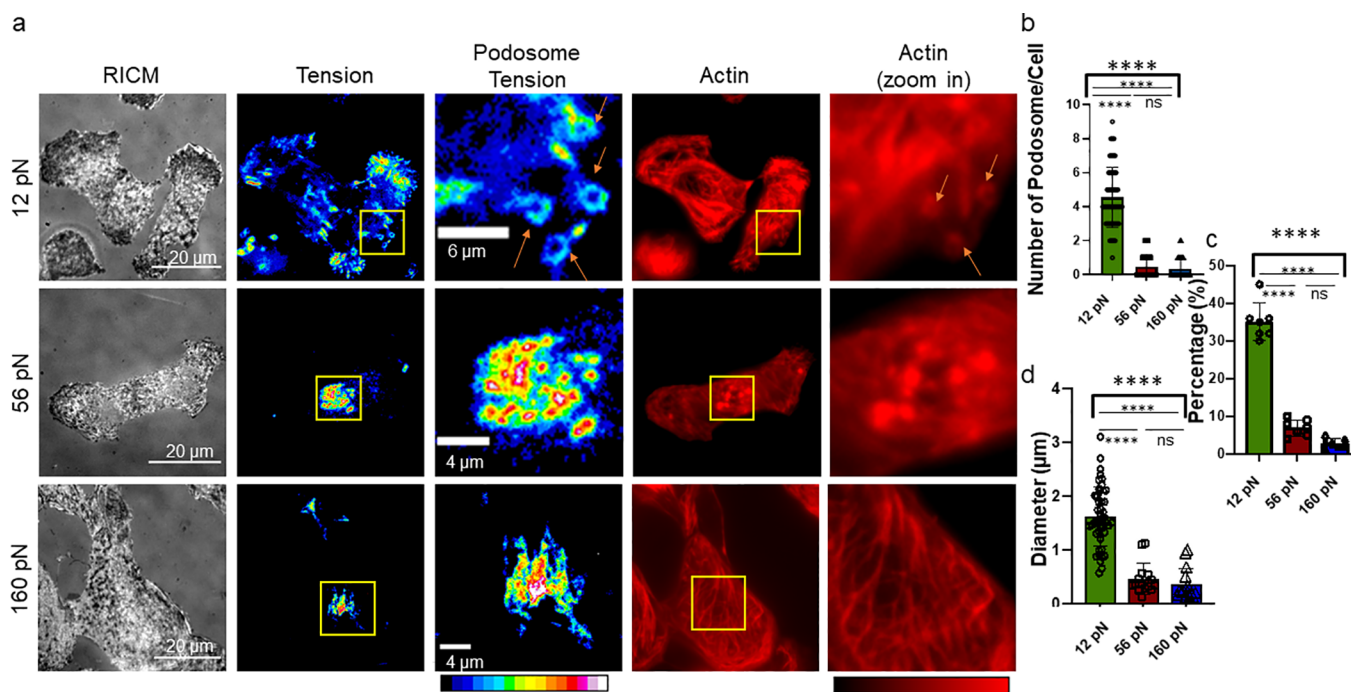


Figure 7. Podosomes/podosome-like organelles as an early maturation marker in CMCs. (a) Representative images of CMCs (fixed) having podosome-like structure on the 12 pN surface ($t = 8–10$ h), RISM showing the cell of interest, TRITC channel showing the podosome tension ring, and Phalloidin staining confirming colocalization of actin in the structure. Scale bar = 20 μm (first column) and 6.4 μm (third column). (b) Number of podosomes in rupture probe surfaces. (c) Percentage of cells having podosomes (where each dot represents one biological replicate, $n = 5$). (d) Diameter distribution of podosomes. Each data point represents a single cell, while the bar shows the average. ****, ***, **, *, and ns indicate $p < 0.0001$, $p < 0.001$, $p < 0.01$, $p < 0.05$, and not significant, respectively, as determined from one-way ANOVA. Error bars show standard deviation for $n > 3$, where each experiment was averaged from three or more different cell isolations with three different sets of surface preparations.

YAP expression and colocalization in cardiac fibroblasts (CF) derived from the same NRVM isolation protocol. Briefly, CF cells were cocultured with CMCs on 12, 56, and 160 pN substrates for 6–8 h and then stained for YAP protein expression. We found that CF total YAP levels were similar for the three probe surfaces tested. However, in agreement with the literature, we found that YAP accumulated in the nucleus at levels that corresponded with mechanical stiffness of the ECM and 160 pN substrates had the greatest YAP nuclear localization followed by 56 and 12 pN surfaces (Figure S19).

Next, we focused on studying the effectors of YAP upregulation in CMCs. Prior literature linked integrin mechanotransduction to YAP translocation/upregulation the ERK/MAPK pathway.^{57,62} MEK (mitogen activated protein kinase kinase) is a key regulator of the ERK/MAPK pathway, which controls the cytosolic YAP expression and nuclear YAP translocation.^{63,64} It has also been shown that inhibition of MEK resulted in significantly lower YAP expression.^{65,66} To better understand the role of MEK in mediating integrin traction forces and YAP mechanosensing, we treated CMCs with U0126, a MEK inhibitor.^{66,67} The treated cells had a significantly lower spread area and rupture density for all three probes tested (Figure S20). There was also a significant reduction of YAP expression as a result of U0126 treatment in CMCs (Figure S21). These results suggest that upregulation of YAP expression is tuned by the magnitude of integrin tension likely through signaling from mature focal adhesions (Figure 6e).

Podosomes as an Early Maturation Marker in CMCs. Prior studies have shown that CMCs form ring-shaped

actomyosin and vinculin rich structures under stress due to hypoxic conditions (O_2 deprivation).⁶⁸ These structures were described as “rosettes” and more recently as podosomes: structures of 0.15–1 μm in diameter with actin-rich cores and cortex domains that contain vinculin, α -actinin, and β_1 integrins.⁶⁸ Podosomes are found in numerous cell types including dendritic cells, T-cells, and vascular smooth muscle cells and have been intensively studied.^{69–72} Nonetheless, very little is known about their functional roles in cardiac cells and what cues trigger podosome formation.^{73–75,87} There has been some speculation that podosomes play an active role in developmental remodeling of the neuromuscular junction, though more work is needed to support this claim.^{69,75} Moreover, some earlier investigations have suggested neural and dendritic cells form podosomes at earlier stages of maturation.⁷⁶

We discovered that $\sim 30\%$ of CMCs seeded on the 12 pN surface formed ring-like patterns of probe rupture with micrometer scale dimensions, and these patterns appeared near the center of the cells (Figure 7a). Interestingly, these tension patterns resembled the tension patterns observed for podosome assemblies reported by Glazier et al.⁷⁷ Podosomes are most often identified by immunostaining of F-actin (central core), vinculin, and talin (at the rim). To verify whether the observed tension pattern was generated by podosomes, cells were stained both with the F-actin stain phalloidin and with vinculin antibodies after culture on probe surfaces of varying mechanical stability (Figure 7a, Figures S22 and S23). Puncta showed the characteristic F-actin core surrounded by a rim of vinculin and integrin tension, thus suggesting the formation of

podosomes (Figures S22 and S23). Podosomes were predominantly observed for cells on 12 pN surfaces with an average of 4 per cell compared to the 56 and 160 pN surfaces that displayed an average of 1–2 podosome per cell (Figure 7a,b). We found that 30% of cells on the 12 pN surfaces had podosomes compared to ~10% of cells on the 56 and 160 pN surfaces that showed podosomes (Figure 7c). These two observations suggest that deficiency in integrin tension and focal adhesion formation is highly correlated with podosome formation. This is consistent with the observation by Yu and Sheetz et al. that fibroblasts cultured on fluid membranes show enhanced podosome formation.⁷⁸ Podosome size was also correlated with integrin tension, and podosomes on 12 pN surfaces showed larger diameters (Figure 7d). Further confirming that podosome formation is mechanosensitive, we found that treatment with ROCK inhibitor led to enhanced formation of podosomes in all substrates tested (Figure S12a). Surprisingly, we also found a strong correlation between podosome formation and twitching. While only ~30% of cells cultured on 12 pN surfaces were beating (Figure 3b), the majority (>90%) of this subpopulation displayed podosomes like puncta (Figure S24). This result along with the literature suggest that podosomes provide alternate adhesion signaling to compensate for weak focal adhesions.

Subsequently, we focused on identifying the timeline of podosome formation. We wanted to know if podosome formation occurs early in CMCs adhesion and then whether these structures mediate twitching or alternatively whether podosomes form in cells that may be more functional and already twitching. To answer this question, we performed time-lapse imaging after seeding cells and noticed that podosome-like puncta formed in cells on 12 pN surfaces at early time points (2–3 h after seeding, Figure S25a). Podosomes seemed to form even before cells were fully elongated, which may indicate their role in aiding in cell spreading on substrates with labile adhesion sites and weak focal adhesion formation. Moreover, prior studies have postulated a role for podosomes in cell–cell junctions.^{70,71,74} To test if cell–cell interactions increase podosome assembly, we plated cells at higher densities to find out if there is more podosome formation with cells which are in proximity. We seeded 76 000 cells/cm² and imaged at the 6–8 h time point (Figure S25b). We found that cells plated at higher densities displayed more podosome-like structures. Podosome size and number were correlated to cell density, and isolated cells displayed the smallest podosomes compared to cells that were in proximity to their neighboring cells (Figure S25c,d). We also observed increased formation of podosome-like structures when ROCK and myosin IIA are inhibited (Figure S26). Taken together, we find that podosome formation is highly mechanosensitive, upstream of the twitching phenotype, and is also sensitive to cell–cell contact.

CONCLUSION

During and after heart failure, a significant number of CMCs die and are lost.^{81,82} The native heart has a limited capacity to recover from this loss by regenerating CMCs from CFs. To facilitate efficient cardiac regeneration after a cardiac arrest, researchers recently have focused on stem cell-based therapeutics.⁸⁰ However, stem cells fail to efficiently recapitulate the phenotype of myocytes which are lost.^{79–81} There is a growing interest in understanding the maturation and differentiation of CMCs to properly mimic the environment of native myocardium.^{4,83} This report addresses how molecular

forces influence the early maturation of CMCs and builds upon the body of work investigating the maturation and development of the cardiovascular system. Our findings have the potential to greatly aid future efforts to harness CMCs as stem cell-based regeneration therapies.

Biomechanical stimuli such as ECM stiffness and matrix rigidity can determine the functional phenotype of cardiac cells during development.^{18–23,80} Here, we describe how tuning integrin forces on the piconewton scale modulate early CMC maturation using nucleic acid-based probes conjugated to fibronectin mimic peptides to target integrins expressed in NRVMs. CMC developmental processes were investigated on three different rupture probes with distinctive mechanical tolerance, T_{tol} (~12, ~56, and ~160 pN), by changing the geometry of force application to the DNA tether.³¹ The 12 and 56 pN probes have been commonly used, and these DNA duplexes denature under tension; in contrast, the 160 pN probe ruptures upon biotin–streptavidin dissociation. The 160 pN probe was designed to expand the range of adhesion ligand rupture thresholds. We initially speculated that ligand T_{tol} with intermediate levels (56 pN) would offer improved CMC maturation compared to the low (12 pN) and high (160 pN) T_{tol} values. This prediction was based on prior work showing that gels with ~10 kPa modulus offered improved CMC maturation compared to gels with lower (1 kPa) or higher modulus (50–100 kPa).^{19,23} Surprisingly, we found that CMCs displayed a similar phenotype on the 160 pN probes compared to the 56 pN rupture probes. While it is difficult to compare molecular rupture thresholds in units of piconewtons to the modulus of a deformable substrate, our findings suggest that increasing T_{tol} from 12 pN to 56 pN/160 pN is analogous to the increasing gel modulus to values that show improved maturation phenotypes. Moreover, the mechanical stability of the 56 pN/160 pN probes leads to stable integrin–RGD bonds that transmit more tension and facilitate CMC maturation. This results in CMCs displaying more elongated morphology, higher spreading area, more periodic and synchronized beating, and more synchronized Ca²⁺ transients on 56 and 160 pN surfaces in contrast to the 12 pN surfaces.

The SR is the contractile unit of cardiomyocytes.³² Elongated, well aligned SR is important for proper contraction of CMCs. Previous literature has shown that the matrix stiffness affects calcium dynamics, SR organization, and contractility of CMCs.^{19,23–25,32,50} It has also been demonstrated that NRVMs seeded on 10 kPa PDMS gels coated with collagen develop well-defined SR organization compared to softer gels (1 and 5 kPa).^{19,23,24,50} Stiffness tunable PDMS micro-post-substrates have also been used to show that greater stiffness of substrates resulted in more organized SR distribution measured by sarcomeric α -actinin alignment.⁵⁰ Our findings demonstrate that DNA probes that offer >56 pN T_{tol} ligands impact CMC development in an analogous way to mechanical signaling arising from increased elastic modulus.

YAP, another regulator of cardiac regeneration, is sensitive to integrin traction forces. However, little is known about how YAP signaling responds to integrin forces in CMC development.⁶⁷ Our findings indicate that pN integrin forces modulate YAP expression (8–10 h) and nuclear translocation (12–14 h), suggesting that YAP contributes to functional maturation of CMCs.

Although previous work suggested that CMCs can form podosomes like organelles on collagen and laminin substrates,⁶⁸ the mechanisms underlying this process have yet to

be described. Our work reveals that CMCs can form podosome-like structures on fibronectin mimetics and demonstrates how the threshold of piconewton integrin forces influence this formation. We find that CMCs mainly form podosome-like structures when the integrin force threshold is low (<12 pN), indicating a relationship between podosome formation and integrin force mediated CMC maturation. Inhibition of ROCK signaling resulted in similar rates of podosome formation on all three substrates, indicating that formation is dependent both on RGD–integrin ligand bond strength and ROCK signaling. Together, this data demonstrates that the specific magnitude of piconewton integrin forces functionally control podosome formation in the early maturation of CMCs. This should inform future studies addressing how specific integrin heterodimers (e.g., β_1 , β_3) influence podosome formation and their specific role in CMCs.^{77,78,87}

One limitation of the current study is the use of glass substrates. Stiff substrates boost cell traction forces and lead to a more fibrotic phenotype when studying CMC maturation.^{19,23} That said, glass and plastic tissue culture dishes are still widely used to study CMC biology (for a list of examples see Supporting Information Table 3) and thus offer a valuable platform to better understand how the adhesion receptor forces modulate CMC maturation. We have also worked to address this problem by integrating the DNA probes into hydrogel substrates with ~10–13 kPa modulus (Figure S27). Unfortunately, CMCs did not spread on these DNA-modified soft substrates within the 8–10 h of seeding, and longer incubation times led to DNA degradation. Nonetheless, in all our experiments, the glass substrate was maintained as a constant and therefore differences in CMC maturation are attributed to the molecular biophysics of DNA rupture thresholds. Another limitation of the current study is that the DNA probes rupture irreversibly, and hence the probe influences the biology and reports cumulative signal over time. Therefore, rupture density cannot be directly compared to other measures of forces such as traction force microscopy or the reversible DNA probes that can measure the steady state tension applied by cells without applying a maximum limit on ligand tension. These DNA rupture probes are best suited to control tension rather than to measure it. Also, as the probes are DNA-based, there is some loss of signal due to nuclease activity, spontaneous DNA duplex dissociation, and biotin–streptavidin dissociation. Nonetheless, the work represents an important step toward developing a molecular level understanding of how adhesion receptor forces tune the process of CMC maturation as measured through physiological and biochemical markers. The general strategy can also be applied to other stem cell subtypes and may be broadly useful in that capacity.

METHODS

DNA Probe Synthesis and Preparation. Rupture probes used in this project were adapted from previous published work.^{34,35} Cyclic peptide Grifka was first coupled to the 5' end of rupture probe (TGT) top strand (12/56 pN ligand strand) via copper catalyzed cycloaddition reaction. cRGDfK-azide was conjugated onto the top strand in 25 μ L of reaction mixture containing 5 mM of sodium ascorbate and 0.1 μ M preformed Cu-THPTA complex. The mixture was allowed to react for 2 h, and the product was purified by reverse phase HPLC. The biotin bottom strands were coupled to Cy3B NHS ester also via NHS-amine coupling. For the biotin rupture probe, cRGD

was coupled first following HPLC purification, and subsequently Cy3B-NHS was conjugated and purified using HPLC.

Surface Preparation. All the DNA probes were immobilized to the surface using biotin–streptavidin interactions. The glass slides were covalently functionalized with the biotin group and further incubated with streptavidin by using previously published literature procedures. Glass coverslips (number 2, 25 mm diameter; VWR) were sonicated in EtOH and subsequently with Nanopure water for 10 min and then etched in piranha solution (a 3:1 mixture of sulfuric acid and hydrogen peroxide) for 10–15 min. The glass coverslips were then washed several times with Nanopure water and EtOH and then were incubated in 1% (3-aminopropyl) triethoxysilane (APTES) in EtOH for 1 h. The substrates were immersed in EtOH three times, subsequently rinsed with EtOH, and dried under nitrogen. Subsequently, substrates were baked in an oven (~100 °C) for 10 min. After cooling, the samples were incubated with NHS-biotin (Thermo Fisher) at 2 mg/mL in DMSO overnight. The substrates were washed with EtOH and dried in an oven for 20 min. The biotin-functionalized glass substrates were assembled into cell chambers, flushed with 1 \times PBS (3 \times 5 mL), incubated with 0.1% BSA (EMD Chemicals, 100 μ g/ μ L, 30 min), and washed again with 1 \times PBS (3 \times 5 mL). Streptavidin was then added (5 μ g/mL for 45 min, room temperature) followed by washing with 1 \times PBS (3 \times 5 mL). The chambers were then incubated with the rupture probes (150 nM) for 1 h and rinsed prior to CMC experiment and imaging.

Cell Isolation. NRVMs were isolated from 2- to 3-day-old neonatal rat pups and cultured as a monolayer as described previously.^{82,84,85} Only the lower one-third of the heart (from the apex to the midline) was excised in order to minimize contaminating atrioventricular nodal cells. Each of the biological replicate cells were isolated from ~20 neonatal rat pups. For all *in vitro* experiments, NRVMs were plated at a density of 25 000–30 000 cells per surface chamber (circular coverslip with a diameter of 16 mm exposed; area = 804 mm²). The cells were cultured in 2% serum for all experiments.

Immunostaining. For staining on rupture probes, CMCs were fixed and stained on 12, 56, and 160 pN probes following 8–10 h of cell spreading. Cells were fixed in 2–4% formaldehyde in 1 \times PBS for 8–10 min. Cells were permeabilized for 3 min with 0.1% Triton X-100 and were blocked with BSA for 30 min. Staining was performed for 1 h at room temperature with 1:1000 Alexa 488-Phalloidin (ab176753, Abcam), 1:50 Vinculin Antibody SF9 647 (sc-73614 AF647, Santa Cruz Biotechnology), 1:50 Phospho-Paxillin (Tyr1888) and Polyclonal Antibody (PAS-17828, Thermo Fisher) followed by 1:5500 Alexa Fluor 555 goat antirabbit (A21147, Thermo Fisher) or 10 μ g/mL α -actinin antibody (PAS-17308) from Invitrogen, thermofisher), 10 μ g/mL SERCA2a Antibody (SC-376235) from Santa Cruz Antibody, or YAP1 (SC 376830) followed by 1:1000 Alexa Fluor 647 or 488 goat antimouse IgG2b (γ 2b) (A28175 or A28181) or goat antirabbit secondary antibody (A27034 or A27080) from Thermo Fisher as indicated in the experiment details. Immunostained cells were imaged using total internal reflection fluorescence microscopy (TIRFM).

Drug Treatment. CMCs were pretreated for (>1 h @RT) with various inhibitors before seeding. Cells were either treated with 25 μ M Y27632 dihydrochloride (Y0503, MilliporeSigma), with 10 μ M eptifibatide (CAS no. 881997-860), with 10 μ M Blebbistatin (18-521, Fisher Scientific), or with 15 μ M of U1026 (PD 98059, cell signaling) for 30 min. We used DMSO as a solvent vehicle for the control group.

Optical Microscopy. Live NRVMs were imaged in 2% serum buffer at 25 °C using a Nikon Eclipse Ti microscope driven by the Elements software package. The microscope is equipped with Evolve electron multiplying charge coupled device (Photometrics), an Intensilight epifluorescence source (Nikon), and a CFI Apo 100 \times NA 1.49 objective (Nikon). It also includes a TIRF launcher with three laser lines: 488 nm (10 mW), 561 nm (50 mW), and 638 nm (20 mW). The microscope also has a perfect focus system which can lock the focus to assist capturing multipoint and time lapse images without losing focus. All of the reported experiments were performed using the following Chroma filter cubes: DAPI, TIRF 488, TIRF 561, FITC, TRITC, Cy5, BF, and RICM.

Calcium Staining and Automated Analysis of ROI Calcium Intensity. CMCs were stained with Fluo-4 (F14210, Thermofisher) using a previously published protocol.⁵⁶ After staining, the CMCs were left in the incubator for 2 h to restore spontaneous twitching. Time lapses were taken in the FITC channel. ROIs were manually selected at the area of calcium sparks. ROIs were analyzed using an automated code in MATLAB 2019b. The average fluorescence intensity and 99th percentile fluorescence intensity of each ROI were both quantified at each time point. The 99th percentile was used to check for saturation of the camera; if any time point for a given ROI had a 99th percentile fluorescence intensity equivalent to the maximum of the detector (255 arbitrary units), the ROI was discarded. ROIs with zero-value 99th percentiles were also discarded.

For each remaining ROI, calcium spikes were identified using a peak finding process. First, the average intensity was normalized to a 901-point median filter with truncated edges using MATLAB's built-in "medfilt" command. Next, MATLAB's built-in "findpeaks" function was used to identify fluorescence intensity spikes with the "MinPeakDistance" and "MinPeakHeight" settings set to 200 and 1.2, respectively. Finally, peaks that occurred at least 100 points after the initial time point and 200 points before the final time point were stored. Specifically, 100 points before the peak and 200 points after the peak were saved.

Peak dynamics were measured by fitting an equation to the saved 301-point intensity vs time curves

$$I = (I_{\max} - I_0) \left(\left(1 - \exp\left(-\frac{t - t_{\text{start}}}{\tau_{\text{rise}}}\right) \right) u(t - t_{\text{start}}) - \left(\exp\left(-\frac{(t - t_{\text{start}} - t_{\text{end}})}{\tau_{\text{fall}}}\right) \right) u(t - t_{\text{start}} - t_{\text{fall}}) \right) + I_0$$

where I_{\max} is the maximum peak intensity (i.e., spike height), I_0 is the baseline intensity, t is the time, t_{start} and t_{end} are the times at which the spikes begin rising and falling, respectively, τ_{rise} and τ_{fall} are the spike rising and falling time constants, respectively, and $u(x)$ is the Heaviside function denoting initiation at time x . Fitting of the parameter set [I_{\max} , I_0 , t_{start} , t_{end} , τ_{rise} , τ_{fall}] was performed using MATLAB's built-in "simultaneous" function with initial guesses of the maximum intensity, the minimum intensity, 50 time points, 100 time points, 5 time points, and 20 time points, respectively. All fit parameters were given a lower and upper bound of 0 and ∞ intensity units, respectively, and fitting was performed with the "HybridFcn" setting set to "fmincon" and all other settings set to their default values. The synchronization time was measured from 10 videos per condition, where each data point represents the synchronization time measured in one video. We calculated the synchronization time as the average time between peaks for ROI ($n > 10$) in the same plane of view, and the lower time means the time differences between peaks are small and the CMC beating has a higher degree of temporal synchronization.

Illustration and Statistical Analysis. All the illustrations of this manuscript were prepared by either adobe illustrator or BioRender.com. Statistical analyses were performed in GraphPad, imagej, Microsoft excel, and MatLab.

ASSOCIATED CONTENT

Supporting Information

The Supporting Information is available free of charge at ACS Nano website. This report includes one supplementary text file and six supplementary videos. The supplementary text contains . The Supporting Information is available free of charge at <https://pubs.acs.org/doi/10.1021/acsnano.1c04303>.

Additional data, statistical analysis, and details on experimental procedures (PDF)

12 pN twitching (AVI)

56 pN twitching (AVI)

160 pN twitching (AVI)

12 pN Ca staining (AVI)

56 pN Ca staining (AVI)

160 pN Ca staining (AVI)

AUTHOR INFORMATION

Corresponding Author

Khalid Salaita – Department of Chemistry, Emory University, Atlanta, Georgia 30322, United States; Wallace H. Coulter Department of Biomedical Engineering, Georgia Institute of Technology and Emory University, Atlanta, Georgia 30332, United States; orcid.org/0000-0003-4138-3477; Email: k.salaita@emory.edu

Authors

Sk Aysha Rashid – Department of Chemistry, Emory University, Atlanta, Georgia 30322, United States

Aaron T. Blanchard – Wallace H. Coulter Department of Biomedical Engineering, Georgia Institute of Technology and Emory University, Atlanta, Georgia 30332, United States

J. Dale Combs – Department of Chemistry, Emory University, Atlanta, Georgia 30322, United States

Natasha Fernandez – Division of Pediatric Cardiology, Department of Pediatrics, Emory University School of Medicine and Children's Healthcare of Atlanta, Atlanta, Georgia 30322, United States

Yixiao Dong – Department of Chemistry, Emory University, Atlanta, Georgia 30322, United States; orcid.org/0000-0001-8943-9842

Hee Cheol Cho – Division of Pediatric Cardiology, Department of Pediatrics, Emory University School of Medicine and Children's Healthcare of Atlanta, Atlanta, Georgia 30322, United States; Wallace H. Coulter Department of Biomedical Engineering, Georgia Institute of Technology and Emory University, Atlanta, Georgia 30332, United States

Complete contact information is available at:

<https://pubs.acs.org/10.1021/acsnano.1c04303>

Author Contributions

Sk A.R. and K.S. conceived of the project. Sk A.R. designed and performed all of the experiments. A.T.B. assisted with automated calcium analysis. J.D.C. helped with automated analysis of actinin staining. A.T.B. and J.D.C. contributed equally. Y.D. assisted with PEG gel experiments. N.F. and H.C. helped with cell isolation and biological assay discussion. K.S. and Sk A.R. wrote the manuscript. All the authors helped revise the manuscript.

Notes

The authors declare no competing financial interest.

ACKNOWLEDGMENTS

This work is supported by NIH NIGMS R01GM124472, NIH NIGMS 1R01GM131099, NHLBI R01HL142866, NHLBI R01HL143065, R01HL147270, R01HL157363, AHA 20TPA35260085, and Department of Defense GRANT12901705 (PR191598). The authors especially want to thank R. Glazier and A. Ramey-Ward for discussion leading to planning of experiments. Also, the authors are grateful to H. Ogasawara for assisting in acquiring mass spectrometry of oligo used in this project. The authors also acknowledge J. Fan's contribution for NRVM isolations.

REFERENCES

- (1) Ishii, Y.; Langberg, J.; Rosborough, K.; Mikawa, T. Endothelial Cell Lineages of the Heart. *Cell Tissue Res.* **2009**, *335* (1), 67–73.
- (2) Rochais, F.; Mesbah, K.; Kelly, R. G. Signaling Pathways Controlling Second Heart Field Development. *Circ. Res.* **2009**, *104* (8), 933–42.
- (3) Wu, S. M.; Chien, K. R.; Mummery, C. Origins and Fates of Cardiovascular Progenitor Cells. *Cell* **2008**, *132* (4), 537–43.
- (4) Guo, Y.; Pu, W. T. Cardiomyocyte Maturation: New Phase in Development. *Circ. Res.* **2020**, *126* (8), 1086–1106.
- (5) Cui, M.; Wang, Z.; Bassel-Duby, R.; Olson, E. N. *Development* **2018**, *145* (24), dev171983.
- (6) Mummery, C. L.; Zhang, J.; Ng, E. S.; Elliott, D. A.; Elefanty, A. G.; Kamp, T. J. Differentiation of Human Embryonic Stem Cells and Induced Pluripotent Stem Cells to Cardiomyocytes: a Methods Overview. *Circ. Res.* **2012**, *111* (3), 344–58.
- (7) Iismaa, S. E.; Kaidonis, X.; Nicks, A. M.; Bogush, N.; Kikuchi, K.; Naqvi, N.; Harvey, R. P.; Husain, A.; Graham, R. M. Comparative Regenerative Mechanisms Across Different Mammalian Tissues. *NPJ Regen Med.* **2018**, *3*, 6.
- (8) Kosmalska, A. J.; Casares, L.; Elosegui-Artola, A.; Thottacherry, J. J.; Moreno-Vicente, R.; Gonzalez-Tarrago, V.; Del Pozo, M. A.; Mayor, S.; Arroyo, M.; Navajas, D.; Trepas, X.; Gauthier, N. C.; Rocacuscachs, P. Physical Principles of Membrane Remodelling During Cell Mechanoadaptation. *Nat. Commun.* **2015**, *6*, 7292.
- (9) Zhao, M. T.; Ye, S.; Su, J.; Garg, V. Cardiomyocyte Proliferation and Maturation: Two Sides of the Same Coin for Heart Regeneration. *Front Cell Dev Biol.* **2020**, *8*, S94226.
- (10) Scuderì, G. J.; Butcher, J. Naturally Engineered Maturation of Cardiomyocytes. *Front Cell Dev Biol.* **2017**, DOI: 10.3389/fcell.2017.00050.
- (11) Kannan, S.; Kwon, C. Regulation of Cardiomyocyte Maturation During Critical Perinatal Window. *J. Physiol* **2020**, *598* (14), 2941–2956.
- (12) Nguyen, P. K.; Neofytou, E.; Rhee, J. W.; Wu, J. C. Potential Strategies to Address the Major Clinical Barriers Facing Stem Cell Regenerative Therapy for Cardiovascular Disease: A Review. *JAMA Cardiol* **2016**, *1* (8), 953–962.
- (13) Denning, C.; Borgdorff, V.; Crutchley, J.; Firth, K. S.; George, V.; Kalra, S.; Kondrashov, A.; Hoang, M. D.; Mosqueira, D.; Patel, A.; Prodanov, L.; Rajamohan, D.; Skarnes, W. C.; Smith, J. G.; Young, L. E. Cardiomyocytes from Human Pluripotent Stem Cells: From Laboratory Curiosity to Industrial Biomedical Platform. *Biochim. Biophys. Acta* **2016**, *1863* (7), 1728–1748.
- (14) Grskovic, M.; Javaherian, A.; Strulovici, B.; Daley, G. Q. Induced Pluripotent Stem Cells—Opportunities for Disease Modelling and Drug Discovery. *Nat. Rev. Drug Discov* **2011**, *10* (12), 915–29.
- (15) Du Pre, B. C.; Doevendans, P. A.; van Laake, L. W. Stem Cells for Cardiac Repair: an Introduction. *J. Geriatr Cardiol* **2013**, *10* (2), 186–197.
- (16) Bellin, M.; Marchetto, M. C.; Gage, F. H.; Mummery, C. L. Induced Pluripotent Stem Cells: The New Patient? *Nat. Rev. Mol. Cell Biol.* **2012**, *13* (11), 713–26.
- (17) Dambrot, C.; Passier, R.; Atsma, D.; Mummery, C. L. Cardiomyocyte Differentiation of Pluripotent Stem Cells and Their Use As Cardiac Disease Models. *Biochem. J.* **2011**, *434* (1), 25–35.
- (18) McCain, M. L.; Parker, K. K. Mechanotransduction: The Role of Mechanical Stress, Myocyte Shape, and Cytoskeletal Architecture on Cardiac Function. *Pflugers Arch* **2011**, *462* (1), 89–104.
- (19) Tallawi, M.; Rai, R.; Boccaccini, A. R.; Aifantis, K. E. Effect of Substrate Mechanics on Cardiomyocyte Maturation and Growth. *Tissue Eng. Part B Rev.* **2015**, *21* (1), 157–65.
- (20) Zhu, R.; Blazeski, A.; Poon, E.; Costa, K. D.; Tung, L.; Boheler, K. R. Physical Developmental Cues for the Maturation of Human Pluripotent Stem Cell-Derived Cardiomyocytes. *Stem Cell Res. Ther* **2014**, *5* (5), 117.
- (21) Keung, W.; Boheler, K. R.; Li, R. A. Developmental Cues for the Maturation of Metabolic, Electrophysiological and Calcium Handling Properties of Human Pluripotent Stem Cell-Derived Cardiomyocytes. *Stem Cell Res. Ther* **2014**, *5* (1), 17.
- (22) Hughes, C. J. R.; Jacobs, J. R. Dissecting the Role of the Extracellular Matrix in Heart Disease: Lessons from the *Drosophila* Genetic Model. *Vet Sci.* **2017**, *4* (2), 24.
- (23) Jacot, J. G.; McCulloch, A. D.; Omens, J. H. Substrate Stiffness Affects the Functional Maturation of Neonatal Rat Ventricular Myocytes. *Biophys. J.* **2008**, *95* (7), 3479–87.
- (24) Boothe, S. D.; Myers, J. D.; Pok, S.; Sun, J.; Xi, Y.; Nieto, R. M.; Cheng, J.; Jacot, J. G. The Effect of Substrate Stiffness on Cardiomyocyte Action Potentials. *Cell Biochem Biophys* **2016**, *74* (4), 527–535.
- (25) Rodriguez, A. G.; Han, S. J.; Regnier, M.; Sniadecki, N. J. Substrate Stiffness Increases Twitch Power of Neonatal Cardiomyocytes in Correlation with Changes in Myofibril Structure and Intracellular Calcium. *Biophys. J.* **2011**, *101* (10), 2455–64.
- (26) Rodriguez, M. L.; Graham, B. T.; Pabon, L. M.; Han, S. J.; Murry, C. E.; Sniadecki, N. J. Measuring the Contractile Forces of Human Induced Pluripotent Stem Cell-Derived Cardiomyocytes with Arrays of Microposts. *J. Biomech Eng.* **2014**, *136* (5), 051005.
- (27) Pandey, P.; Hawkes, W.; Hu, J.; Megone, W. V.; Gautrot, J.; Anilkumar, N.; Zhang, M.; Hirvonen, L.; Cox, S.; Ehler, E.; Hone, J.; Sheetz, M.; Iskratsch, T. Cardiomyocytes Sense Matrix Rigidity through a Combination of Muscle and Non-muscle Myosin Contractions. *Dev Cell* **2018**, *44* (3), 326–336.
- (28) Lyon, R. C.; Zanella, F.; Omens, J. H.; Sheikh, F. Mechanotransduction in Cardiac Hypertrophy and Failure. *Circ. Res.* **2015**, *116* (8), 1462–1476.
- (29) Hidalgo, C.; Donoso, P. Cell Signaling. Getting to the Heart of Mechanotransduction. *Science* **2011**, *333* (6048), 1388–90.
- (30) Wang, X.; Ha, T. Defining Single Molecular Forces Required to Activate Integrin and Notch Signaling. *Science* **2013**, *340* (6135), 991–4.
- (31) Zhang, Y.; Qiu, Y.; Blanchard, A. T.; Chang, Y.; Brockman, J. M.; Ma, V. P.-Y.; Lam, W. A.; Salaita, K. Platelet Integrins Exhibit Anisotropic Mechanosensing and Harness Piconewton Forces to Mediate Platelet Aggregation. *Proc. Natl. Acad. Sci. U. S. A.* **2018**, *115* (2), 325–330.
- (32) Galie, P. A.; Khalid, N.; Carnahan, K. E.; Westfall, M. V.; Stegemann, J. P. Substrate Stiffness Affects Sarcomere and Costamere Structure and Electrophysiological Function of Isolated Adult Cardiomyocytes. *Cardiovasc Pathol* **2013**, *22* (3), 219–27.
- (33) Lammerding, J.; Kamm, R. D.; Lee, R. T. Mechanotransduction in Cardiac Myocytes. *Ann. N.Y. Acad. Sci.* **2004**, *1015*, 53–70.
- (34) Liu, Y.; Galiour, K.; Ma, V. P.; Salaita, K. Molecular Tension Probes for Imaging Forces at the Cell Surface. *Acc. Chem. Res.* **2017**, *50* (12), 2915–2924.
- (35) Zhang, Y.; Ge, C.; Zhu, C.; Salaita, K. DNA-Based Digital Tension Probes Reveal Integrin Forces During Early Cell Adhesion. *Nat. Commun.* **2014**, *5*, 5167.
- (36) Kapp, T. G.; Rechenmacher, F.; Neubauer, S.; Maltsev, O. V.; Cavalcanti-Adam, E. A.; Zarka, R.; Reuning, U.; Notni, J.; Wester, H. J.; Mas-Moruno, C.; Spatz, J.; Geiger, B.; Kessler, H. A Comprehensive Evaluation of the Activity and Selectivity Profile of Ligands for RGD-binding Integrins. *Sci. Rep* **2017**, *7*, 39805.
- (37) Paolini, P.; Pick, D.; Lapira, J.; Sannino, G.; Pasqualini, L.; Ludka, C.; Sprague, L. J.; Zhang, X.; Bartolotta, E. A.; Vazquez-Hidalgo, E.; Barba, D. T.; Bazan, C.; Hardiman, G. Developmental and Extracellular Matrix-Remodeling Processes in Rosiglitazone-Exposed Neonatal Rat Cardiomyocytes. *Pharmacogenomics* **2014**, *15* (6), 759–74.
- (38) Israeli-Rosenberg, S.; Manso, A. M.; Okada, H.; Ross, R. S. Integrins and Integrin-Associated Proteins in the Cardiac Myocyte. *Circ. Res.* **2014**, *114* (3), 572–586.
- (39) Ogawa, E.; Saito, Y.; Harada, M.; Kamitani, S.; Kuwahara, K.; Miyamoto, Y.; Ishikawa, M.; Hamanaka, I.; Kajiyama, N.; Takahashi, N.; Nakagawa, O.; Masuda, I.; Kishimoto, I.; Nakao, K. Outside-In Signalling of Fibronectin Stimulates Cardiomyocyte Hypertrophy in

Cultured Neonatal Rat Ventricular Myocytes. *J. Mol. Cell Cardiol* **2000**, *32* (5), 765–76.

(40) Neiman, G.; Scarafia, M. A.; La Greca, A.; Santin Velazque, N. L.; Garate, X.; Waisman, A.; Mobbs, A. M.; Kasai-Brunswick, T. H.; Mesquita, F.; Martire-Greco, D.; Moro, L. N.; Luzzani, C.; Bastos Carvalho, A.; Sevelever, G. E.; Campos de Carvalho, A.; Guberman, A. S.; Miriuka, S. G. Integrin Alpha-5 Subunit Is Critical for the Early Stages of Human Pluripotent Stem Cell Cardiac Differentiation. *Sci. Rep* **2019**, *9* (1), 18077.

(41) Sarrazy, V.; Koehler, A.; Chow, M. L.; Zimina, E.; Li, C. X.; Kato, H.; Caldarone, C. A.; Hinz, B. Integrins Alpha5 and Alpha3 Promote Latent TGF-Beta1 Activation by Human Cardiac Fibroblast Contraction. *Cardiovasc. Res.* **2014**, *102* (3), 407–17.

(42) Graf, K.; Neuss, M.; Stawowy, P.; Hsueh, W. A.; Fleck, E.; Law, R. E. Angiotensin II and Alpha(V)Beta(3) Integrin Expression in Rat Neonatal Cardiac Fibroblasts. *Hypertension* **2000**, *35* (4), 978–84.

(43) Balasubramanian, S.; Quinones, L.; Kasiganesan, H.; Zhang, Y.; Pleasant, D. L.; Sundararaj, K. P.; Zile, M. R.; Bradshaw, A. D.; Kuppuswamy, D. Beta3 Integrin in Cardiac Fibroblast Is Critical for Extracellular Matrix Accumulation During Pressure Overload Hypertrophy in Mouse. *PLoS One* **2012**, *7* (9), e45076.

(44) Terracio, L.; Rubin, K.; Gullberg, D.; Balog, E.; Carver, W.; Jyring, R.; Borg, T. K. Expression of Collagen Binding Integrins During Cardiac Development and Hypertrophy. *Circ. Res.* **1991**, *68* (3), 734–44.

(45) Jurchenko, C.; Chang, Y.; Narui, Y.; Zhang, Y.; Salaita, K. S. Integrin-Generated Forces Lead to Streptavidin-Biotin Unbinding in Cellular Adhesions. *Biophys. J.* **2014**, *106* (7), 1436–46.

(46) Estevez, B.; Shen, B.; Du, X. Targeting Integrin And Integrin Signaling in Treating Thrombosis. *Arterioscler Thromb Vasc Biol.* **2015**, *35* (1), 24–9.

(47) Wang, S. Q.; Song, L. S.; Lakatta, E. G.; Cheng, H. Ca²⁺ Signalling between Single L-Type Ca²⁺ Channels and Ryanodine Receptors in Heart Cells. *Nature* **2001**, *410* (6828), 592–6.

(48) Oyehaug, L.; Loose, K. O.; Jolle, G. F.; Røe, A. T.; Sjaastad, I.; Christensen, G.; Sejersted, O. M.; Louch, W. E. Synchrony of Cardiomyocyte Ca²⁺ Release Is Controlled by T-Tubule Organization, SR Ca²⁺ Content, and Ryanodine Receptor Ca²⁺ Sensitivity. *Biophys. J.* **2013**, *104* (8), 1685–1697.

(49) Martewicz, S.; Serena, E.; Zatti, S.; Keller, G.; Elvassore, N. Substrate and Mechanotransduction Influence SERCA2a Localization in Human Pluripotent Stem Cell-Derived Cardiomyocytes Affecting Functional Performance. *Stem Cell Res.* **2017**, *25*, 107–114.

(50) Corbin, E. A.; Vite, A.; Peyster, E. G.; Bhoopalam, M.; Brandimarto, J.; Wang, X.; Bennett, A. I.; Clark, A. T.; Cheng, X.; Turner, K. T.; Musunuru, K.; Margulies, K. B. Tunable and Reversible Substrate Stiffness Reveals a Dynamic Mechanosensitivity of Cardiomyocytes. *ACS Appl. Mater. Interfaces* **2019**, *11* (23), 20603–20614.

(51) Velayutham, N.; Alfieri, C. M.; Agnew, E. J.; Riggs, K. W.; Baker, R. S.; Ponny, S. R.; Zafar, F.; Yutzey, K. E. Cardiomyocyte Cell Cycling, Maturation, and Growth by Multinucleation in Postnatal Swine. *J. Mol. Cell Cardiol* **2020**, *146*, 95–108.

(52) Milliron, H. Y.; Weiland, M. J.; Kort, E. J.; Jovinge, S. Isolation of Cardiomyocytes Undergoing Mitosis With Complete Cytokinesis. *Circ. Res.* **2019**, *125* (12), 1070–1086.

(53) Botting, K. J.; Wang, K. C.; Padhee, M.; McMillen, I. C.; Summers-Pearce, B.; Rattanaraj, L.; Cutri, N.; Posterino, G. S.; Brooks, D. A.; Morrison, J. L. Early Origins of Heart Disease: Low Birth Weight and Determinants of Cardiomyocyte Endowment. *Clin. Exp. Pharmacol. Physiol.* **2012**, *39* (9), 814–23.

(54) Liu, Z.; Yue, S.; Chen, X.; Kubin, T.; Braun, T. Regulation of Cardiomyocyte Polyploidy and Multinucleation By Cyclin1. *Circ. Res.* **2010**, *106* (9), 1498–506.

(55) Landim-Vieira, M.; Schipper, J. M.; Pinto, J. R.; Chase, P. B. Cardiomyocyte Nuclearity and Ploidy: When Is Double Trouble? *J. Muscle Res. Cell Motil* **2020**, *41* (4), 329–340.

(56) Dupont, S. Role of YAP/TAZ in Cell-Matrix Adhesion-Mediated Signalling and Mechanotransduction. *Exp. Cell Res.* **2016**, *343* (1), 42–53.

(57) Elbediwy, A.; Thompson, B. J. Evolution of Mechanotransduction via YAP/TAZ in Animal Epithelia. *Curr. Opin Cell Biol.* **2018**, *51*, 117–123.

(58) Yamashiro, Y.; Thang, B. Q.; Ramirez, K.; Shin, S. J.; Kohata, T.; Ohata, S.; Nguyen, T. A. V.; Ohtsuki, S.; Nagayama, K.; Yanagisawa, H. Matrix Mechanotransduction Mediated by Thrombospondin-1/Integrin/YAP in the Vascular Remodeling. *Proc. Natl. Acad. Sci. U. S. A.* **2020**, *117* (18), 9896–9905.

(59) Elosegui-Artola, A.; Andreu, I.; Beedle, A. E. M.; Lezamiz, A.; Uroz, M.; Kosmalska, A. J.; Oria, R.; Kechagia, J. Z.; Rico-Lastres, P.; Le Roux, A. L.; Shanahan, C. M.; Trepast, X.; Navajas, D.; Garcia-Manyès, S.; Roca-Cusachs, P. Force Triggers YAP Nuclear Entry by Regulating Transport Across Nuclear Pores. *Cell* **2017**, *171* (6), 1397–1410.e14.

(60) Mo, J. S.; Park, H. W.; Guan, K. L. The Hippo Signaling Pathway in Stem Cell Biology and Cancer. *EMBO Rep* **2014**, *15* (6), 642–56.

(61) Boopathy, G. T. K.; Hong, W. Role of Hippo Pathway-YAP/TAZ Signaling in Angiogenesis. *Front Cell Dev Biol.* **2019**, DOI: 10.3389/fcell.2019.00049.

(62) Vite, A.; Zhang, C.; Yi, R.; Emms, S.; Radice, G. L. Alpha-Catenin-Dependent Cytoskeletal Tension Controls Yap Activity in the Heart. *Development* **2018**, *145* (5), dev149823.

(63) Shaul, Y. D.; Seger, R. The MEK/ERK Cascade: from Signaling Specificity to Diverse Functions. *Biochim. Biophys. Acta* **2007**, *1773* (8), 1213–26.

(64) Zhang, W.; Liu, H. T. Mapk Signal Pathways in the Regulation of Cell Proliferation in Mammalian Cells. *Cell Res.* **2002**, *12* (1), 9–18.

(65) Li, L.; Wang, J.; Zhang, Y.; Zhang, Y.; Ma, L.; Weng, W.; Qiao, Y.; Xiao, W.; Wang, H.; Yu, W.; Pan, Q.; He, Y.; Sun, F. Mek1 Promotes Yap and Their Interaction Is Critical for Tumorigenesis in Liver Cancer. *FEBS Lett.* **2013**, *587* (24), 3921–7.

(66) Ramey-Ward, A. N.; Su, H.; Salaita, K. Mechanical Stimulation of Adhesion Receptors Using Light-Responsive Nanoparticle Actuators Enhances Myogenesis. *ACS Appl. Mater. Interfaces* **2020**, *12* (32), 35903–35917.

(67) Zheng, M.; Jacob, J.; Hung, S. H.; Wang, J. The Hippo Pathway in Cardiac Regeneration and Homeostasis: New Perspectives for Cell-Free Therapy in the Injured Heart. *Biomolecules* **2020**, *10* (7), 1024.

(68) Hilenski, L. L.; Terracio, L.; Borg, T. K. Myofibrillar and Cytoskeletal Assembly in Neonatal Rat Cardiac Myocytes Cultured on Laminin and Collagen. *Cell Tissue Res.* **1991**, *264* (3), 577–87.

(69) Sit, B.; Feng, Z.; Xanthis, I.; Marhuenda, E.; Zingaro, S.; Shanahan, C.; Jones, G. E.; Yu, C.-h.; Iskratsch, T. Matrix Stiffness and Blood Pressure Together Regulate Vascular Smooth Muscle Cell Phenotype Switching and Cofilin Dependent Podosome Formation. *bioRxiv*, 2020, DOI: 10.1101/2020.12.27.424498.

(70) Kaverina, I.; Stradal, T. E.; Gimona, M. Podosome Formation in Cultured A7r5 Vascular Smooth Muscle Cells Requires Arp2/3-Dependent De-Novo Actin Polymerization at Discrete Microdomains. *J. Cell Sci.* **2003**, *116* (24), 4915–4924.

(71) Linder, S.; Wiesner, C. Tools of the Trade: Podosomes As Multipurpose Organelles of Monocytic Cells. *Cell. Mol. Life Sci.* **2015**, *72* (1), 121–35.

(72) Linder, S.; Kopp, P. Podosomes at a glance. *J. Cell Sci.* **2005**, *118* (10), 2079–2082.

(73) Zhu, X.; Efimova, N.; Arnette, C.; Hanks, S. K.; Kaverina, I. Podosome Dynamics and Location in Vascular Smooth Muscle Cells Require CLASP-Dependent Microtubule Bending. *Cytoskeleton (Hoboken)* **2016**, *73* (6), 300–15.

(74) Bernadzki, K. M.; Rojek, K. O.; Proszynski, T. J. Podosomes in Muscle Cells and Their Role in the Remodeling of Neuromuscular Postsynaptic Machinery. *Eur. J. Cell Biol.* **2014**, *93* (10–12), 478–85.

(75) Burgstaller, G.; Gimona, M. Podosome-Mediated Matrix Resorption and Cell Motility in Vascular Smooth Muscle Cells. *Am. J. Physiol. Heart Circ Physiol* **2005**, *288* (6), H3001–5.

(76) Cougoule, C.; Lastrucci, C.; Quiet, R.; Mascarau, R.; Meunier, E.; Lugo-Villarino, G.; Neyrolles, O.; Poincloux, R.; Maridonneau-Parini, I. Podosomes, But Not the Maturation Status, Determine the Protease-Dependent 3D Migration in Human Dendritic Cells. *Front Immunol* **2018**, DOI: 10.3389/fimmu.2018.00846.

(77) Glazier, R.; Brockman, J. M.; Bartle, E.; Mattheyses, A. L.; Destaing, O.; Salaita, K. DNA Mechanotechnology Reveals that Integrin Receptors Apply pN Forces in Podosomes on Fluid Substrates. *Nat. Commun.* **2019**, *10* (1), 4507.

(78) Yu, C. H.; Law, J. B.; Suryana, M.; Low, H. Y.; Sheetz, M. P. Early Integrin Binding to Arg-Gly-Asp Peptide Activates Actin Polymerization and Contractile Movement that Stimulates Outward Translocation. *Proc. Natl. Acad. Sci. U. S. A.* **2011**, *108* (51), 20585–90.

(79) Garbern, J. C.; Lee, R. T. Cardiac Stem Cell Therapy and the Promise of Heart Regeneration. *Cell Stem Cell* **2013**, *12* (6), 689–98.

(80) Duellen, R.; Sampaolesi, M. Stem Cell Technology in Cardiac Regeneration: A Pluripotent Stem Cell Promise. *EBioMedicine* **2017**, *16*, 30–40.

(81) Ghirelli, A.; Piccoli, M.; Cirillo, F.; Monasky, M. M.; Ciconte, G.; Pappone, C.; Anastasia, L. Cell-Based Therapies for Cardiac Regeneration: A Comprehensive Review of Past and Ongoing Strategies. *Int. J. Mol. Sci.* **2018**, *19* (10), 3194.

(82) Grijalva, S. I.; Gu, J. M.; Li, J.; Fernandez, N.; Fan, J.; Sung, J. H.; Lee, S. Y.; Herndon, C.; Buckley, E. M.; Park, S. J.; Fenton, F. H.; Cho, H. C. Engineered Cardiac Pacemaker Nodes Created by TBX18 Gene Transfer Overcome Source-Sink Mismatch. *Adv. Sci. (Weinh)* **2019**, *6* (22), 1901099.

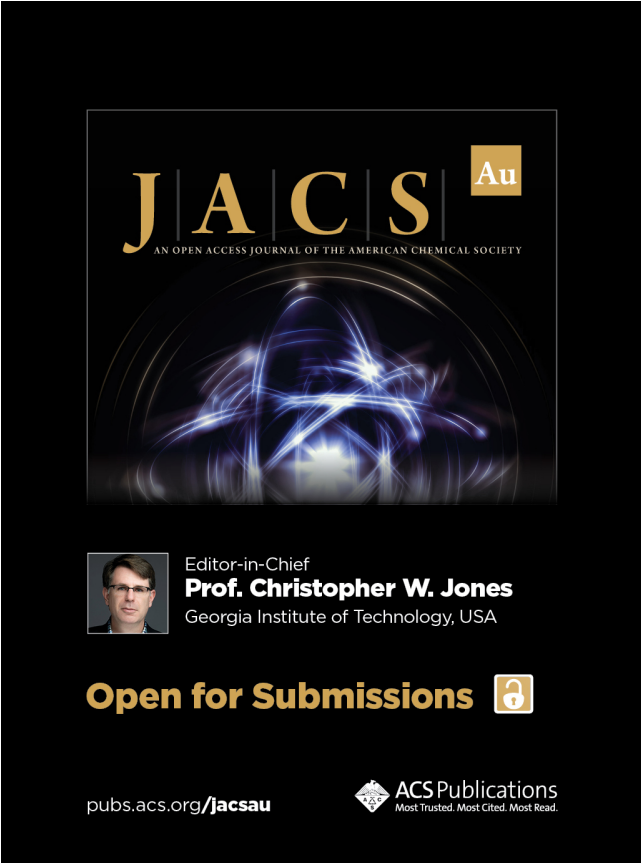
(83) Karbassi, E.; Fenix, A.; Marchiano, S.; Muraoka, N.; Nakamura, K.; Yang, X.; Murry, C. E. Cardiomyocyte Maturation: Advances in Knowledge and Implications for Regenerative Medicine. *Nat. Rev. Cardiol* **2020**, *17* (6), 341–359.

(84) Kapoor, N.; Liang, W.; Marban, E.; Cho, H. C. Direct Conversion of Quiescent Cardiomyocytes to Pacemaker Cells by Expression of Tbx18. *Nat. Biotechnol.* **2013**, *31* (1), 54–62.

(85) Kapoor, N.; Galang, G.; Marban, E.; Cho, H. C. Transcriptional Suppression of Connexin43 By TBX18 Undermines Cell-Cell Electrical Coupling in Postnatal Cardiomyocytes. *J. Biol. Chem.* **2011**, *286* (16), 14073–9.


(86) Cameron, M.; Kekesi, O.; Morley, J. W.; Tapson, J.; Breen, P. P.; van Schaik, A.; Buskila, Y. Calcium Imaging of AM Dyes Following Prolonged Incubation in Acute Neuronal Tissue. *PLoS One* **2016**, *11* (5), e0155468.


(87) Sit, B.; Gutmann, D.; Iskratsch, T. Costameres, Dense Plaques and Podosomes: The Cell Matrix Adhesions in Cardiovascular Mechanosensing. *J. Muscle Res. Cell Motil* **2019**, *40* (2), 197–209.



JACS Au
AN OPEN ACCESS JOURNAL OF THE AMERICAN CHEMICAL SOCIETY

Editor-in-Chief
Prof. Christopher W. Jones
Georgia Institute of Technology, USA

Open for Submissions 

pubs.acs.org/jacsau  ACS Publications
Most Trusted. Most Cited. Most Read.